Chemical heterogeneity and approaches to its control in BiFeO3- BaTiO3 lead-free ferroelectrics

DOI:
10.1039/C7TC04122E

Document Version
Accepted author manuscript

Journal of
Materials Chemistry C

Accepted Manuscript

This article can be cited before page numbers have been issued, to do this please use: I. Calisir and D. Hall, *J. Mater. Chem. C*, 2017, DOI: 10.1039/C7TC04122E.

ROYAL SOCIETY OF CHEMISTRY

rsc.li/materials-c

View Article Online
DOI: 10.1039/C7TC04122E

Chemical heterogeneity and approaches to its control in $BiFeO_3$-$BaTiO_3$ lead-free ferroelectrics

Ilkan Calisir*, David A. Hall

School of Materials, University of Manchester, M13 9PL, Manchester, UK

*Corresponding Author: ilkan.calisir@manchester.ac.uk

View Article Online
DOI: 10.1039/C7TC04122E

ABSTRACT

1 mol% MnO_2 was used to improve electrical resistivity of lead-free $0.75BiFeO_3$-$0.25BaTiO_3$ (75BFBT) ferroelectric ceramics; the materials were perovskite structured with major rhombohedral (*R3c*) phase. The method of incorporation of MnO_2 was found to exert a significant influence on the structure, microstructure and electrical properties. Chemical heterogeneity in the form of core-shell grain microstructures was observed when MnO_2 was added into the undoped calcined powder, in contrast to the relatively homogeneous materials that resulted from adding MnO_2 into the precursor oxide mixture prior to calcination. Compositionally graded regions were detected across the grains consisting of a BF–rich core and BF–depleted shell.

The occurrence of core-shell type microstructures led to various characteristic features including a high cubic phase fraction, contrast between ordered ferroelectric domain configurations in the rhombohedral core and the relatively featureless pseudo-cubic shell, constrained ferroelectric domain switching, and two distinct anomalies in dielectric permittivity at temperatures of 485 and 635˚C. The latter features are attributed to separate phase transitions in the relaxor ferroelectric shell and normal ferroelectric core regions respectively. The application of a thermal quenching procedure caused the formation of ferroelectric domain structures throughout the microstructure and resulted in dramatically enhanced ferroelectric switching behaviour. For example, the remanent polarisation of the as-sintered 75BFBT ceramic increased from 0.06 to 0.31 C m^{-2} after air-quenching. These effects are tentatively attributed to nanoscale phase segregation in the shell region of the as-sintered ceramics, resulting from thermodynamic immiscibility between the BF and BT solid solutions.

View Article Online
DOI: 10.1039/C7TC04122E

1. INTRODUCTION

Bismuth ferrite (BF) and its solid solution systems have been the subject of intensive research, due to its attractive combination of high ferroelectric Curie temperature (~825 °C),[1] high remanent polarisation (~100 μC cm^{-2} in single crystal along the pseudo-cubic $[111]_{pc}$ direction[1] and ~20 μC cm^{-2} in bulk form[2]) and multiferroic behaviour.[1,3] Due to its promising multifunctional properties, considerable research has focused recently on the recognised issues of high leakage current and the synthesis of single-phase $BiFeO_3$ without impurities.[1,3,4]

The origin of high conductivity in $BiFeO_3$ has been a controversial issue, but recent findings have theoretically[5] and experimentally[6–8] confirmed that the conduction mechanism for $BiFeO_3$ synthesised in air (oxygen-rich) is p-type. Based on this observation, the conductivity is attributed to the incorporation of excess oxygen (filling some oxygen vacancies) and the associated formation of electron holes. This can then lead to the conversion of Fe^{2+} ions to Fe^{3+} and Fe^{3+} ions to Fe^{4+}.[8] It was also found that decreasing partial oxygen pressure during synthesis led to a shift from p-type to n-type in $(Bi_{0.5}K_{0.5})TiO_3$–modified $BiFeO_3$.[8] Conversely, for Ca^{2+} (acceptor)-doped $BiFeO_3$ it was found that sintering in a N_2 atmosphere induced a transition from a p-type semiconductor to oxide ion conductor.[7]

According to the binary phase diagram of the Bi_2O_3-Fe_2O_3 system, it has been noted that a stable single pure $BiFeO_3$ phase can be obtained only within a narrow temperature range, which can lead to the formation of secondary phases such as $Bi_2Fe_4O_9$, $Bi_{25}FeO_{39}$, and $Bi_{36}Fe_2O_{57}$.[2,9,10] These reported obstacles have been overcome using various processing methods including mechanochemical synthesis,[2] rapid liquid phase sintering,[11] sol-gel method,[12] microwave synthesis,[13] chemical leaching,[14] annealing under magnetic field[15] *etc.* Furthermore, *site engineering* has been applied to $BiFeO_3$ by partial substitutions of A- and B-site ions in the $BiFeO_3$ perovskite structure,[16] including rare earth ions substituted for Bi^{3+},[17–23] and transition metal ions for Fe^{3+}.[24–28] In addition, solid solution formation with other ABO_3-type perovskite ceramics leads to binary,[29–34] ternary[35–37] or even quaternary[38] compounds.

Although $BiFeO_3$-$PbTiO_3$ in particular has been reported to show superior properties, rising environmental concerns on the usage of lead-based ceramics[39–41] have led to extensive research on lead-free solid solution combinations. Among them, $BiFeO_3$-$BaTiO_3$ (BF-BT) ceramics have been intensively studied as promising candidates for lead-free, high temperature ceramics. Nonetheless, the main focus of such research was primarily concerned with the magnetic properties due to the observation of weak ferromagnetism at room temperature. Subsequently, the dielectric, ferroelectric and piezoelectric properties have been explored and received considerable attention, particularly for high temperature applications.[37,42]

Despite improvements in the synthesis of single perovskite phase BF-BT ceramics, well-saturated P-E loops and low dielectric loss are rarely reported without any further modification,[30] due to the presence of a relatively high leakage current. Therefore, many

View Article Online
DOI: 10.1039/C7TC04122E

researchers have employed additional aliovalent dopants in order to increase its insulation behaviour. Among these, it has been found that a small amount of Mn has a beneficial effect on the electrical properties of $BiFeO_3$-based ceramics.[30,43–47] However, Mn is a transition metal that can exhibit various valence states (Mn^{2+}, Mn^{3+} and Mn^{4+}) depending on the oxygen partial pressure during heat treatment.[48,49]

The influence of Mn on the properties of $BiFeO_3$-based compounds has been systematically studied and it has been concluded that determination of the optimum amount of Mn is crucial, since excessive amounts are found to cause deterioration of the electrical resistivity due to increasing valence fluctuations generating extrinsic oxygen vacancies.[43] Generally it was found that 0.1-0.6 *wt*% MnO_2 addition has a positive effect on increasing the resistivity. However, Mn was incorporated into the compositions in various different ways, including addition to the pre-calcined compositions as a sintering aid,[30,43,50–52] as a substitution on to the Fe-site[11,46] or as an excess addition into other starting precursor powders.[44,53–56] This raises some uncertainty about the origins of the observed variations in the reported ferroelectric (remanent polarisation, coercive field), dielectric properties (relative permittivity, tanδ and T_C), and structural as well as microstructural features.

Although extensive research has been carried out on Mn-doped $BiFeO_3$-$BaTiO_3$, no single study has addressed the issue of which addition route could be the most beneficial in terms of sintering, resistivity, ferroelectric and dielectric properties. Therefore, we aimed to clarify this point by evaluating different Mn-addition strategies. For this study, the $0.75BiFeO_3$-$0.25BaTiO_3$ composition was selected to be doped with 1 mol% Mn (equivalent to ≈0.3 *wt*%) due to its reported promising properties[30] and major rhombohedral phase existence,[57] which can help to provide a clear indication of the influence of the Mn incorporation route on structural distortions. The doped ceramics exhibited highly insulating behaviour with interesting features, which were found to depend on the doping strategy employed; these included highly saturated or pinched P-E loops, multiple or single peaks in the dielectric permittivity-temperature relationship and homogeneous or heterogeneous microstructure leading to core-shell type grain formation. It is shown that the cooling rate plays a key role in determining the level of chemical heterogeneity and subsequently the functional properties.

View Article Online
DOI: 10.1039/C7TC04122E

2. EXPERIMENTAL PROCEDURES

Undoped and Mn-doped $0.75BiFeO_3$-$0.25BaTiO_3$ (75BFBT) ceramics were synthesized by the conventional solid state reaction method. Bi_2O_3 (99%, Alfa Aesar), Fe_2O_3 (99%, Sigma Aldrich), $BaCO_3$ (99%, Alfa Aesar) and TiO_2 (99%, Fisher Scientific) were used as starting powders for undoped 75BFBT ceramics and MnO_2 (99%, Fluka Chemica) was added as a modifier. 2 mol% Bi_2O_3 excess was added into all compositions to compensate for the loss of this volatile oxide during high temperature heat treatment. This level of bismuth excess was determined as the minimum required to avoid the formation of Fe-rich secondary phases. Two different Mn-incorporation routes were utilised, denoted as *Mn-BC* (1 mol% MnO_2 added as excess in the mixed oxide precursor powders before calcination), *Mn-AC* (1 mol% MnO_2 added as excess in the pre-reacted and milled 75BFBT powder). In the case of Mn-BC, we suppose that the added Mn could be incorporated in solid solution, while for Mn-AC there may be a tendency for segregation in the grain boundary region.

The precursor oxides were weighed according to the required stoichiometric ratios followed by mixing/milling for 24 h using propan-2-ol and yttria-stabilized zirconia media. The milled powders were dried at 85°C overnight followed by calcination at 850°C for 2 h. The calcined powders were milled again for 24 h to reduce the particle size down to the sub-micron region. Polyethylene glycol (PEG) solution as a lubricant was added at a concentration of 2 *wt*% of the dry weight of the powder into the calcined powders to improve compaction behaviour. The calcined powders were uniaxially cold-pressed at around 150 MPa into 8 mm diameter pellets. The pellets were placed on a layer of calcined powder having the same composition to reduce the volatilisation of Bi_2O_3 and to avoid reaction with the supporting alumina plate. Burn-out of the organic additive was achieved by holding at a temperature of 600°C for 1 h, following which the ceramics were sintered at temperatures between 990 and 1050°C for 2-4 h in air, using a heating and cooling rate of 5°C/min. The *as-sintered* ceramics were annealed at 750°C for 15 min, then directly quenched to room temperature, referred to below as *air-quenched*.

High resolution synchrotron x-ray powder diffraction (SXPD) patterns were recorded on the I11 powder diffraction beamline at the Diamond light source. The crushed powders of samples were placed in a glass capillary tube, and the data were collected at ambient temperature in the 2Θ range of 5−100° using the position sensitive detector (PSD). The x-ray photon wavelength was 0.494951 Å. Rietveld analysis of the data was undertaken using TOPAS *v*5 software. For the refinement, ICSD#15299 and ICSD#67518 were used for *R3c* rhombohedral and *Pm-3m* cubic phase, respectively.

The sintered pellets were ground using 800, 1200, 2500 and 4000 grade SiC paper and then polished with 3, 1 and 0.25 μm diamond paste followed by diluted OP-S silica colloidal suspension. Well-polished samples were chemically etched by immersing into the etchant solution (95% distilled water + 4% HCl + 1% HF) for 5 seconds. Microstructures of as-sintered and air-quenched surfaces were examined using a Philips XL30 FEGSEM equipped

View Article Online
DOI: 10.1039/C7TC04122E

with EDS. The average grain size was determined by the linear intercept method over an area of approximately 4400 μm^2 using a multiplication factor of 1.56.[58]

Prior to electrical measurements, the samples were polished to obtain smooth and parallel surfaces. In order to achieve a sufficiently high electric field for the ferroelectric hysteresis measurements, the thickness of the samples was polished down to 0.5 mm. For dielectric and polarisation-electric field (P-E) hysteresis measurements, silver electrode paste (C2000107P3, Gwent Group) was applied on the top and bottom surfaces and then fired at 600°C for 20 minute. For the *air-quenched* ceramics, an air-dried silver paint (AGG3691, Agar Scientific, UK) was applied onto both surfaces of the pellets at room temperature in order to avoid changes in the effects induced by quenching.

Ferroelectric P-E hysteresis measurements were carried out using a function generator (HP 33120A) connected to a Chevin Research HV amplifier to generate the desired high voltage. The samples were subjected to 4 cycles of a sinusoidal electric field with a frequency of 2 Hz. The measured current waveform was integrated numerically over time to yield charge and hence the polarisation was calculated as the surface charge density.[59] Dielectric measurements were carried out at fixed frequencies from 1 to 100 kHz over the temperature range from 25 to 670 °C using a HP 4284A Impedance analyser and a desktop computer which was operated by LabView-based program. The measurements were conducted in air using a heating rate of 2 °C/min.

View Article Online
DOI: 10.1039/C7TC04122E

3. RESULTS and DISCUSSION

3.1 Structural characterization

Full-pattern Rietveld refinement was performed to determine the crystal structures of undoped and Mn-doped ceramic powders. Figure 1 shows the XRD refinements of the undoped 75BFBT, Mn-BC, Mn-AC and air-quenched Mn-AC, while the crystallographic parameters derived from the refinements are summarized in Table 1. Undoped 75BFBT and Mn-BC ceramics predominantly consist of *R3c* rhombohedral phase with phase fractions of 96.5% and 90.3% respectively, the remainder being cubic *Pm-3m*. For the case of as-sintered and air-quenched Mn-AC, the phase fraction of *Pm-3m* was significantly higher in Mn-AC, indicated by the increase in intensity of the reflection at approximately 12.3 °2θ in Figure 1(c), whilst the *R3c* phase fraction increased from 53.6% to 70% as a result of air-quenching , as shown in Figure 1(d). It is apparent that as a small amount of MnO_2 is added into the calcined composition (Mn-AC), it causes significant structural transformations and the formed phases are also highly sensitive to further thermal treatment procedures such as air-quenching.

By examining the involved cations in order to find the origin of such structural changes induced by Mn, it is considered that Bi^{3+} and Ba^{2+} occupy the A-site, while Fe^{3+}, Ti^{4+} and a small amount of multivalent Mn occupy the B-site of the perovskite structure. These cations have different Pauling's electronegativities and ionic radii. The ionic radii of the B-site ions are reported as Ti^{4+}(0.605 Å), Fe^{3+}(0.645 Å), Mn^{4+}(0.53 Å), Mn^{3+}(0.645 Å) and Mn^{2+}(0.83 Å).[60] The ionic radii of Mn in both 4+ and 3+ valence states are within the range of sizes of Fe^{3+} and Ti^{4+}, which could enter the lattice without distorting the structure. However, the ionic size of Mn^{2+} is relatively large compared to that of Fe^{3+} and Ti^{4+}. Thus, Mn^{2+} could enter into either the A- or B-sites. On the other hand, it has been reported that Mn^{4+} is unstable at high temperatures, therefore the valence state of Mn regardless of starting compound can be considered as a mixture of 3+ and 2+ depending on the oxygen environment.[48]

It is also reported that the incorporation of 25 mol% of $BaTiO_3$ into $BiFeO_3$ causes a slight reduction of the rhombohedral distortion and the presence of a small amount of pseudo-cubic phase.[57] Further additions induce a transformation from rhombohedral to pseudo-cubic relaxor ferroelectric phase over a wide range of composition in the solid solution system due to the large ionic size mismatch and charge difference between Bi^{3+}(1.03 Å) and Ba^{2+}(1.35 Å) at the A-site.[57] Our results also confirm that undoped 75BFBT exhibits a predominantly rhombohedral phase, as depicted in Figure 1(a) and Table 1. The effect of adding Mn ions on the crystal structure of BF-BT, specifically the transformation from predominantly *R3c* to a mixture of coexisting *R3c* and *Pm-3m* phases, cannot be explained purely on the basis of the ionic substitution. Instead, we interpret this effect as being due to the development of core-shell (rhombohedral-cubic) type microstructures in the Mn-doped ceramics, as discussed further below.

View Article Online
DOI: 10.1039/C7TC04122E

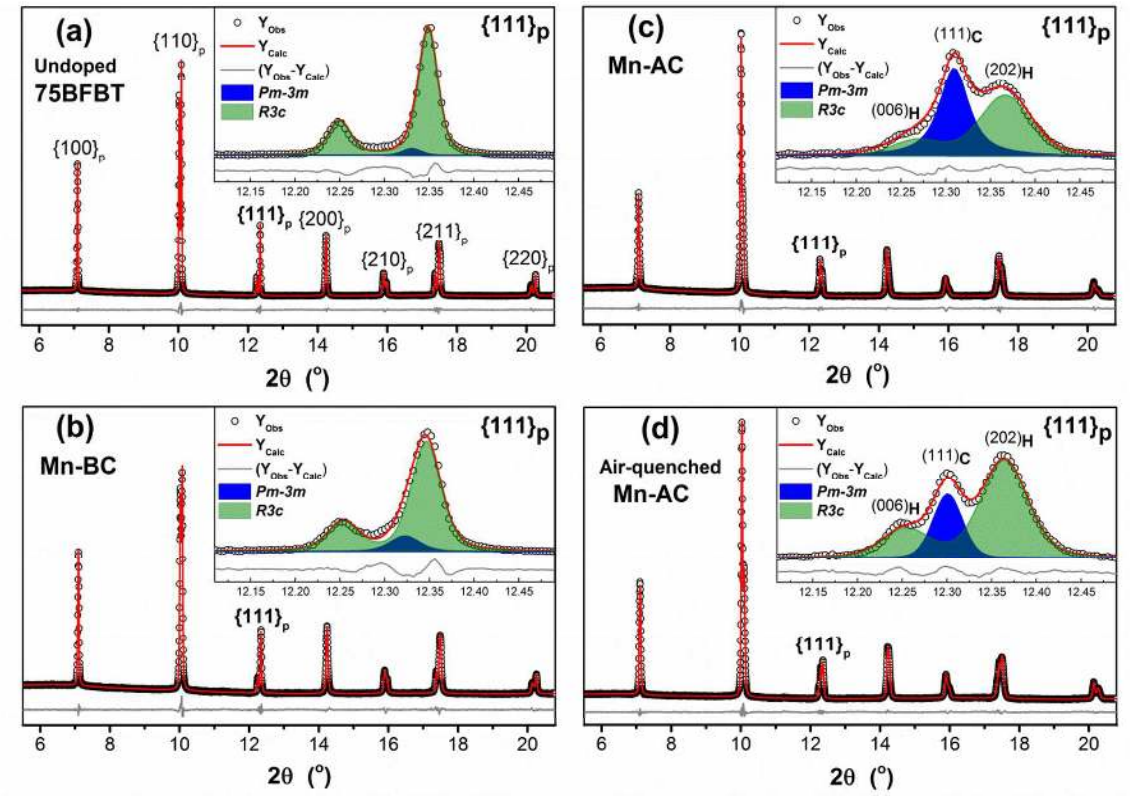

Figure 1. High resolution SXPD patterns of undoped and Mn-doped 75BFBT ceramics. The fitting results of refined structures for **a)** undoped 75BFBT, **b)** Mn-BC, **b)** Mn-AC and **d)** air-quenched Mn-AC ceramics. The insets show the $\{111\}_p$ peak profiles in relation to rhombohedral, *R3c* (the reflection of $(006)_H$ and $(202)_H$ in hexagonal setting), and single (111) reflection of cubic, *Pm-3m*, phases.

For the refinement of the Mn-AC powder, several binary phase models were considered in order to fit the broad asymmetric peaks; the best fitting was achieved by a combination of *R3c* rhombohedral + *Pm-3m* cubic, as noted above. In spite of the improvement relative to the single phase models, broad asymmetry was still present in the peak profiles for certain reflections, which was tentatively attributed to anisotropic strain. To verify this assumption, Stephenson's model[61] was applied to these data during Rietveld refinement and an improved fit was obtained, as can be seen in the insets of Figure 1(c)-(d) for the $\{111\}_p$ peak. Microstructural observations, described in section 3.2 below, indicate the presence of core-shell type grains in the ceramics, which may be the source of the anisotropic strain and the associated peak broadening. It has been suggested that chemical heterogeneity in the form of core-shell structures can introduce internal stresses and lead to broad asymmetric peaks.[62,63]

View Article Online
DOI: 10.1039/C7TC04122E

Table 1: Structural parameters of undoped 75BFBT and Mn-doped ceramics obtained from Rietveld refinement. *Goodness of fit (*GoF*) is the value of R_{wp}/R_{exp}.

Parameters	Undoped 75BFBT		Mn-BC		Mn-AC		Air-quenched Mn-AC	
Phases	*R3c*	*Pm-3m*	*R3c*	*Pm-3m*	*R3c*	*Pm-3m*	*R3c*	*Pm-3m*
Fraction, %	96.5(1)	3.5(1)	90.3(6)	9.7(6)	53.6(5)	46.4(5)	70.(4)	30.0(4)
Unit cell parameters, Å								
a	5.6241(1)	3.9866(2)	5.6245(3)	3.9867(2)	5.6158(6)	3.9932(4)	5.6158(4)	3.9957(3)
c	13.9009(5)	= a	13.8939(8)	= a	13.8784(15)	= a	13.8939(10)	= a
Cell volume, Å^3	380.78(3)	63.363(8)	380.65(5)	63.445(12)	379.05(8)	63.670(2)	379.47(6)	63.792(14)
R-factors								
R_{wp}	3.23		3.26		3.2		3.33	
R_{exp}	1.56		1.59		1.71		1.53	
GoF*	2.07		2.04		1.87		2.18	

Similar observations were made previously by Lennox *et al.*[64] on the basis of neutron diffraction studies on $BiFeO_3$-$KNbO_3$ solid solutions. It was suggested that regions consisting of different A-site and B-site ion ratios, as a consequence of chemical inhomogeneity, can lead to peak broadening. Dolgos *et al.*[65] also reported large thermal parameters in $0.75Bi(Fe_{2/8}Ti_{3/8}Mg_{3/8})O_3$-$0.25BaTiO_3$ for the oxygen and A-site cations which is associated with considerable local strain as confirmed by diffuse scattering in the electron diffraction patterns. Our results are supportive of the argument that Bi:Ba and Fe:Ti:Mn ratios may vary in the core and shell regions resulting in local strain within the grains.

3.2 Microstructure

Figure 2 shows the microstructures of polished surfaces for undoped and Mn-doped 75BFBT ceramics sintered at 990°C for 4 h. The results clearly show that the grain size of 75BFBT can be considerably affected by a small amount of Mn addition. Comparing Figures 2(a) and (b), it is evident that a slight decrease in grain size (from 11.9 to 8.8 μm), with a relatively uniform grain size distribution, was observed for Mn-BC ceramics. This could be attributed to enhanced distribution of Mn when it is added as a precursor powder. On the other hand, systematic studies[44,53,55] show that increasing Mn content above this level generally causes significant grain growth in $BiFeO_3$-$BaTiO_3$ ceramics and degradation of electrical resistivity.

The incorporation of excess MnO_2, introduced as an additive prior to calcination, in solid solution can be understood in terms of the defect chemistry of the $BiFeO_3$-based system, as follows. Firstly, we should recognise that some loss of bismuth oxide is expected during the high temperature calcination and sintering stages, leading to the formation of bismuth and oxygen vacancies.[8]

$$2Bi_{Bi}^{x} + 3O_{O}^{x} \rightarrow 2V_{Bi}^{'''} + 3V_{O}^{\bullet\bullet} + Bi_2O_3(g) \quad (1)$$

View Article Online
DOI: 10.1039/C7TC04122E

This provides a mechanism for the incorporation of excess oxygen, leading to p-type electronic conductivity.

$$2V_O^{\bullet\bullet} + O_2(g) \rightarrow 2O_O^x + 4h^{\bullet} \quad (2)$$

The volatilisation of bismuth oxide during processing is commonly compensated by providing an excess in the starting composition, which was 2 mol% in the present case. For Mn-BC, the reaction of part of the excess bismuth oxide with manganese oxide facilitates the formation of the solid solution during the calcination stage. We assume that the manganese is incorporated in the form of Mn^{3+} or Mn^{2+} due to the instability of Mn^{4+} ions at high temperatures.[49] The former case involves isovalent substitution, while in the latter acceptor-type defects with charge-compensating oxygen vacancies are formed. The overall reactions for isovalent and aliovalent (acceptor-type) incorporation, which include the reduction of Mn^{4+} to either Mn^{3+} or Mn^{2+}, are represented in equations (3) and (4) respectively.

$$2Bi_2O_3 + 4MnO_2 \rightarrow 4Bi_{Bi}^x + 4Mn_{Fe}^x + 12O_O^x + O_2(g) \quad (3)$$

$$Bi_2O_3 + 2MnO_2 \rightarrow 2Bi_{Bi}^x + 2Mn_{Fe}^{/} + 5O_O^x + V_O^{\bullet\bullet} + O_2(g) \quad (4)$$

Subsequently, Mn^{2+} ions can be converted to Mn^{3+} by trapping electron holes,[49] leading to a reduction in p-type electronic conductivity and therefore improved insulation resistance, as observed in many studies.[30,43,53]

$$Mn_{Fe}^{/} + h^{\bullet} \rightarrow Mn_{Fe}^x \quad (5)$$

According to the above argument, the incorporation of the added MnO_2 in solid solution requires the presence of excess bismuth oxide (Equations 3 and 4). For Mn-AC, the reaction between the bismuth and manganese oxides could be hindered by the volatilisation of bismuth oxide during sintering, since there was no available opportunity for reaction during a separate calcination stage. In such a case, the incorporation mechanism for additional MnO_2 must involve the formation of additional bismuth and oxygen vacancies, which would reduce the solubility dramatically. The corresponding isovalent and aliovalent (acceptor-type) incorporation mechanisms are represented in equations (6) and (7) respectively.

$$4MnO_2 \rightarrow 4V_{Bi}^{///} + 4Mn_{Fe}^x + 6O_O^x + 6V_O^{\bullet\bullet} + O_2(g) \quad (6)$$

$$4MnO_2 \rightarrow 4V_{Bi}^{///} + 4Mn_{Fe}^{/} + 4O_O^x + 8V_O^{\bullet\bullet} + 2O_2(g) \quad (7)$$

In contrast to the case of Mn-BC, grain growth was greatly suppressed in the Mn-AC ceramic, as illustrated in Figure 2(c); the average grain size was determined as 3.6 μm. This could be associated with segregation of Mn near grain boundaries, creating pinning centres that restrict grain growth during sintering. Therefore, the inhibited grain growth and associated formation of core-shell structures for Mn-AC can be understood on the basis of the reduced solubility of manganese oxide and its effect on grain growth. It was also previously reported that the grain growth can be hindered by the excess Mn accumulated at the grain

View Article Online
DOI: 10.1039/C7TC04122E

boundaries, when MnO_2 is added into pre-calcined compositions followed by sintering.[43,47] In the present study, it was found that increasing the milling time for the Mn-AC powder had little effect on the microstructure of the sintered ceramic, indicating that the production of finer particles could not induce a significant improvement in chemical homogeneity when the MnO_2 was added after the initial calcination reaction.

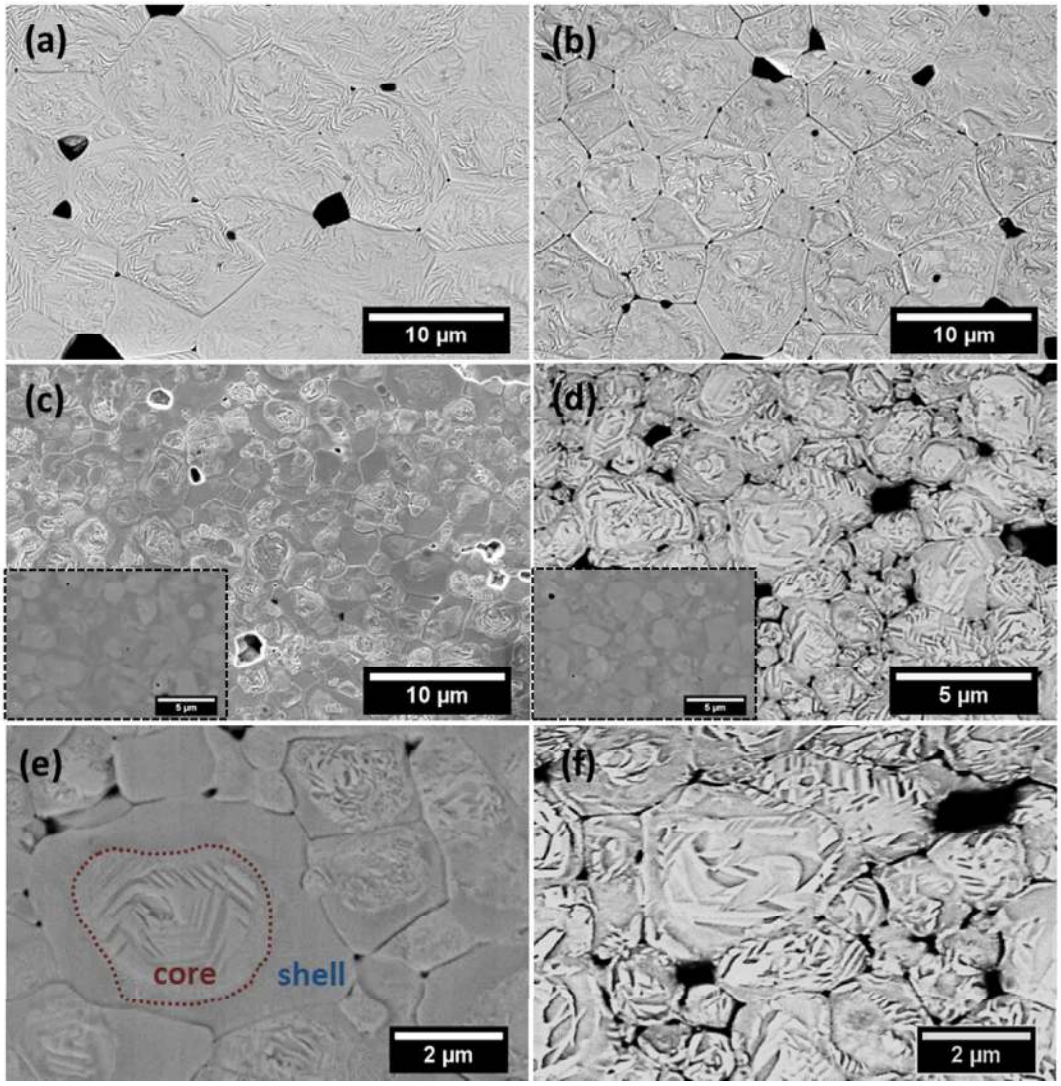

Figure 2. SEM images of chemically etched surfaces of **a)** undoped 75BFBT, **b)** Mn-BC, **c)** Mn-AC ceramics and **d)** air-quenched Mn-AC. Inset images in **(c)** and **(d)** show non-etched sections of the as-sintered and air-quenched ceramics under backscattered imaging mode in SEM (scale bar of inset image is 5 μm). Images **e)** and **f)** illustrate expanded views of core-shell structure in Mn-AC and widespread domain structures in air-quenched Mn-AC.

It is evident that chemically etched undoped 75BFBT and Mn-BC ceramics display clear and homogeneous domain distributions across the grains as seen in Figure 2(a) and (b), whilst the grains of Mn-AC seem partially etched, as shown in Figure 2(c) and (e). A heterogeneous domain distribution was also observed, with domains occurring only at the core of grains. This was not observed in Mn-BC or undoped ceramic. It was first thought that this effect

View Article Online
DOI: 10.1039/C7TC04122E

could be due to the artefacts of chemical etching; therefore, in order to eliminate the etchant effect, the surface was examined without any etching as shown in the inset of Figure 2(c). In Mn-AC ceramics the greyscale contrast of the SEM micrographs, being related to the average atomic numbers, indicated the occurrence of microscale chemical segregation in the form of a core shell structure.

Prior to discussion of elemental analysis relating to the observed elemental micro-segregation, it is worth comparing the as-sintered (Figures 2(c-e)) and air-quenched (Figure 2(d-f)) microstructures for Mn-AC. It is evident that the domain distributions across the grains in the quenched Mn-AC are relatively more homogeneous in comparison with the as-sintered case. It should be noted that both samples were mounted on the same resin mould and etched simultaneously in order to prevent any etching-related microstructural variations. Therefore, it is confirmed that the chemical heterogeneity, which leads to the formation of core-shell type grain structures in the ceramics, is modified by air-quenching. The development of more homogeneous ferroelectric domain structures, achieved by quenching in Mn-AC, may also be responsible for improved ferroelectric properties, as discussed in section 3.4 below.

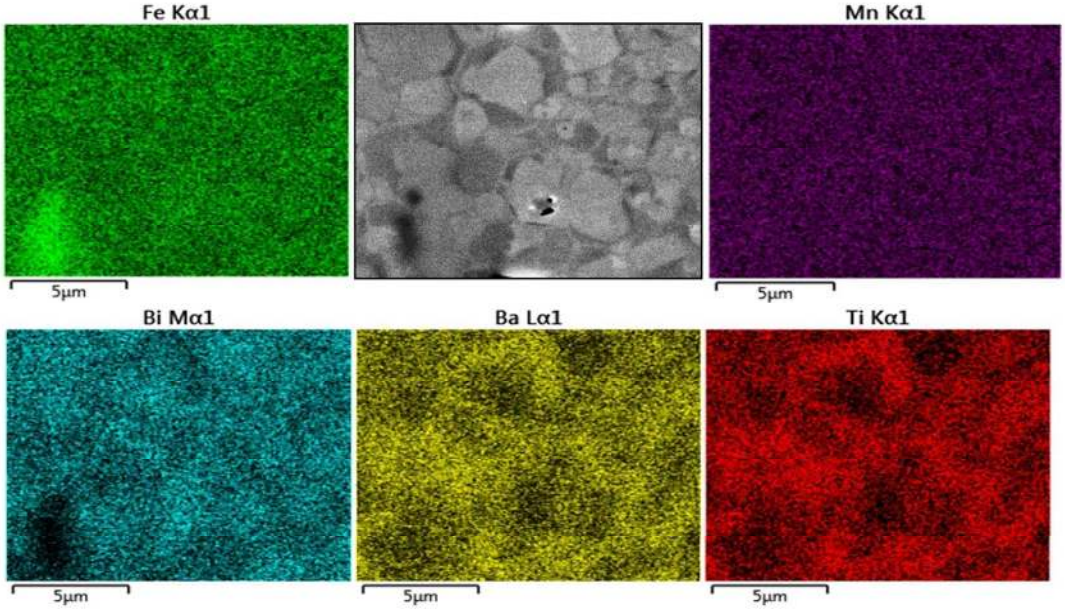

Figure 3. The SEM-EDS elemental mapping results of Mn-AC ceramics sintered at 1050°C for 2h exhibiting core-shell grains.

The SEM-Energy Dispersive Spectroscopy (SEM-EDS) elemental mapping results of non-etched, as-sintered Mn-AC ceramics are illustrated in Figure 3. It can be clearly seen that Ba and Ti signals are weaker in the brighter regions of the SEM image, associated with the grain cores, under secondary electron mode (also confirmed for backscattered electron imaging mode, Figure S1 in the supporting information). Conversely, Bi and Fe elements exhibited a slightly increased intensity in the same brighter areas. The results obtained for the Mn distribution were relatively noisy and uninformative due to the low concentrations. These results indicate that the observed core-shell like structures in Mn-AC are associated with the

View Article Online
DOI: 10.1039/C7TC04122E

micro-segregation of Ba and Ti elements into the shell regions, while Bi and Fe are more concentrated in the core regions. A small amount of Fe-rich secondary phase was also identified, which has been reported in other $BiFeO_3$–based ceramics,[2,25] as highlighted by the Fe elemental map. It should be noted that the SEM-EDS studies were performed on the sample with a relatively short measurement time (1 min.) in order to avoid the volatilisation of Bi due to irradiation.

It was suggested above that when MnO_2 is added into the calcined powder, for Mn-AC, it accumulates in the grain boundary region and can inhibit grain-growth. Therefore, the formation of the core-shell structure may be indirectly linked to Mn addition since the ratio of shell thickness to grain size will be larger when the grain size is smaller. In previous work, the formation of core-shell microstructures was attributed to either kinetic or thermodynamic factors.[66] For the former case, it can be argued that the $BiFeO_3$-rich grain cores are formed first due to the higher reactivity of the constituent oxides, with the $BaTiO_3$-rich shell being incorporated at a later stage of sintering. Such a situation is supported by the observation that the core-shell structure is favoured when grain growth is suppressed. The presence of MnO_2 has the effect of retarding grain growth and interferes with chemical homogenisation during sintering. Hence, we suppose that the formation of the core-shell structure is driven by kinetic factors related to differences in reactivity[66,67] and/or diffusivity of the oxide components.[68]

Thermodynamic immiscibility in the $BiFeO_3$-$BaTiO_3$ system could also play a role in modifying the structure and resulting properties of the pseudo-cubic shell phase. During slow cooling, the presence of a region of immiscibility would provide a driving force for chemical segregation that becomes more pronounced as the temperature is reduced.[38,69] This could lead to nanoscale chemical heterogeneity in the shell regions after slow cooling. The effect of air quenching can be understood on the basis that such nanoscale phase separation is avoided or reduced, providing that the quenching temperature lies near to or above the region of immiscibility.

3.3 Dielectric Properties

The temperature dependence of dielectric permittivity, ε_r and loss, tanδ, as a function of frequency for Mn-doped 75BFBT ceramics is illustrated by the results presented in Figure 4. It is evident that the Mn-BC ceramic exhibits a relatively sharp peak in ε_r at 570 ^oC, which is characteristic of a conventional ferroelectric and indicates the Curie temperature, T_C, corresponding to the transition from the ferroelectric to paraelectric state on heating. Both the permittivity and loss appeared to increase at temperatures above 600 °C, particularly when measured at low frequencies; these effects are attributed to increasing electrical conductivity and the associated space-charge polarisation.[70] For Mn-AC ceramics, the ε_r–T results measured at 100 kHz indicate an increase in T_C to approximately 635 °C. Furthermore, an additional frequency-dependent dielectric peak became apparent at lower temperatures (350 to 500 °C), which is characteristic of a relaxor ferroelectric contribution.

View Article Online
DOI: 10.1039/C7TC04122E

We propose that the unusual dielectric behaviour of the Mn-AC ceramic is a direct consequence of the core-shell microstructure, since it is anticipated that the core and shell regions will exhibit different types of thermally-induced ferroelectric phase transformations, both of which contribute to the overall measured dielectric response. It was shown in section 3.2 above that the core and shell regions in the Mn-AC ceramic are either $BiFeO_3$-rich or $BiFeO_3$-depleted, respectively. In a previous study, it was found that BF-BT ceramics with relatively high BT contents tend to exhibit more diffuse phase transitions.[71,72] Therefore, the low-temperature peak in dielectric permittivity can be tentatively attributed to the contribution from the shell region. The frequency-dependent behaviour of this contribution is consistent with the presence of polar nano-regions and a relaxor ferroelectric character. The presence of a pseudo-cubic phase (Figure 1(c)) and a relatively featureless shell microstructure (Figure 2(e)) provide further evidence to support this argument, since both of these points to the presence of polar nanoregions having pseudocubic symmetry in the shell region. The slight increase in T_C, from 570 to 635 °C, for the higher temperature dielectric peak is consistent with a contribution from the ferroelectric core region, within which the BF-content for Mn-AC is enhanced relative to Mn-BC.

In previous studies, Kiyanagi *et al.*[32] suggested that the observed broad relaxation in dielectric permittivity for BF-BT solid solutions is related to influence of a cubic phase coexisting with the rhombohedral phase. This proposition was supported by Rietveld analysis of XRD data and verified by Ozaki's TEM investigation.[73] In other reports, the occurrence of multiple anomalies in the ε_r –T relationships for $BiFeO_3$-based solid solutions have been attributed to the influence of polymorphic phase transitions,[35] magnetic-electric dipole interactions,[1,74] depolarisation processes,[30] Maxwell-Wagner relaxation[75] and thermodynamic immiscibility of two ferroelectric phases during sintering.[38,69] The development of chemical heterogeneity, in the form of core-shell microstructures, introduces further complexity in the processing-structure-property relationships of such materials but also provides further opportunities for controlling their functional properties.

View Article Online
DOI: 10.1039/C7TC04122E

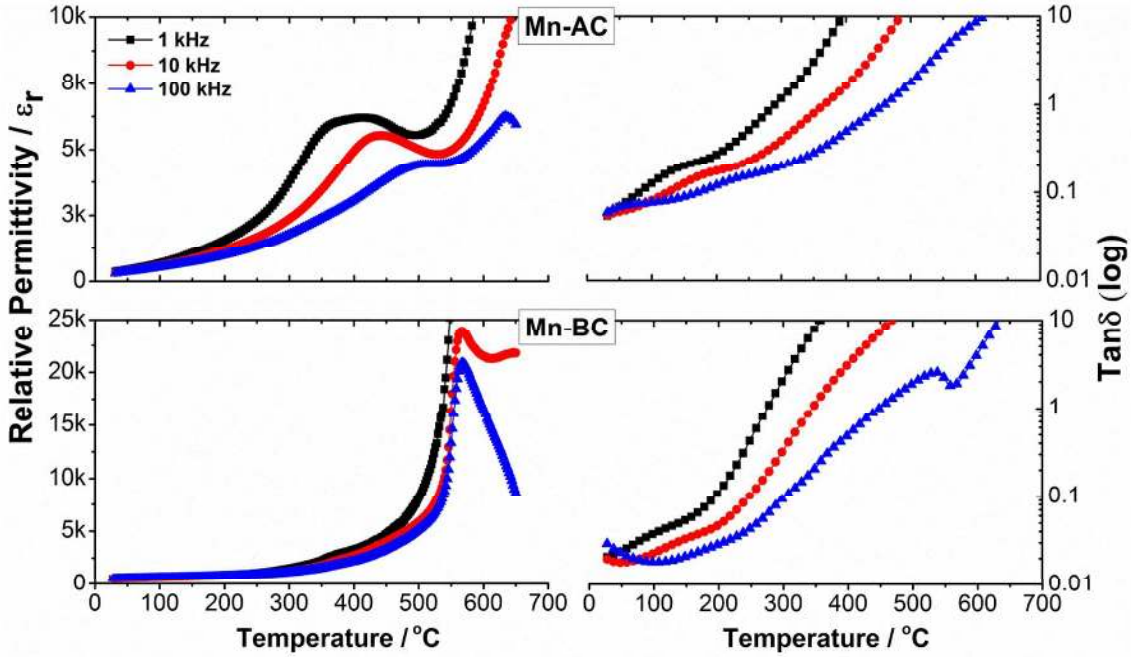

Figure 4. ε_r –T and tan δ–T relationships for Mn-AC and Mn-BC ceramics as a function of frequency.

The influence of air-quenching on the dielectric properties of the Mn-AC ceramics is illustrated in Figure 5(a), which compares the ε_r–T relationships of the as-sintered and air-quenched ceramics. For the Mn-AC ceramic, the main effect of air-quenching was an enhancement of the low-temperature shoulder on the dielectric peak, which developed into a clearly defined second peak. The frequency dispersion of the lower-temperature dielectric peak (represented by ΔT_{Max}) was also reduced after quenching, as shown in Figure 5(b) and Table 2. These results demonstrate that air-quenching had a profound impact on the structure of the shell and is consistent with the transformation from nanopolar to conventional long-range ordered ferroelectric state. The influence of quenching on the ferroelectric ordering within the shell region could be explained by the presence of a region of thermodynamic immiscibility, as noted above in section 3.2. Further studies using high resolution TEM are necessary to establish whether evidence can be found to identify changes in nanoscale chemical segregation associated with variations in cooling rate.

Table 2. Transition temperatures for the corresponding regions of T_{High} and T_{Low} in the as-sintered and air-quenched (15 min and 21 h) Mn-AC ceramics**.** The degree of frequency dispersion was given based on the formula of $\Delta T_{Max} = (T_{Max}^{100\ kHz} - T_{Max}^{1\ kHz})$

	As-sintered	**Air-Quenched**	
	Sintering condition	*Holding time at 750°C*	
	990°C-4 h	15 min	21 h
T_{Low} at 100 kHz	482°C	484°C	510°C
T_{High} at 100 kHz	635°C	639°C	-
ΔT_{Max} for T_{Low}	102°C	33°C	25°C

View Article Online
DOI: 10.1039/C7TC04122E

The occurrence of two strong dielectric anomalies in the ε_r–T plot for the air-quenched Mn-AC ceramic indicates that the underlying chemical heterogeneity, in the form of the core-shell microstructure, is still present after quenching. To verify the stability of the chemical heterogeneity associated with the core-shell structure, the annealing time at 750°C was increased to 21 h, followed by air-quenching. The results, presented in Figure 5(c), show that the two dielectric anomalies largely merged into one broad peak although the inflection in the ε_r–T curve around 630 °C suggests that the underlying contribution from the core is still present. Furthermore, microstructural examination suggested that the core-shell features still persisted after annealing for 21 h, as illustrated in Figures S2 and S3.

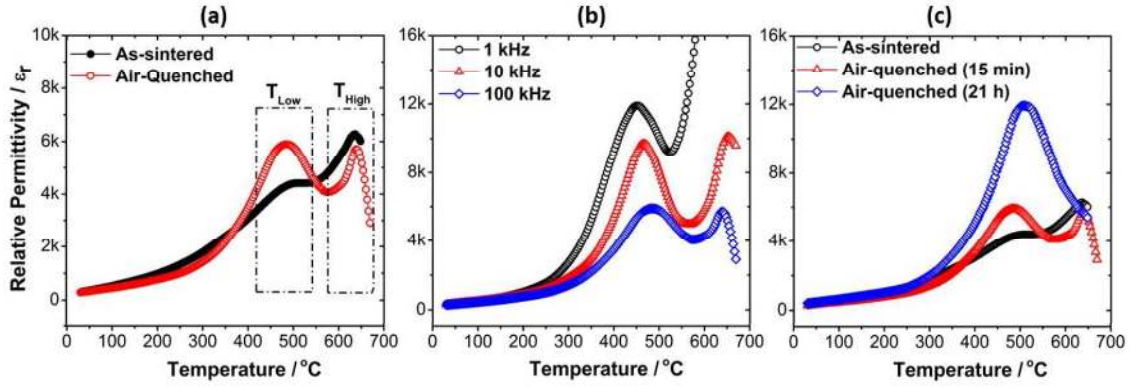

Figure 5. ε_r –T relationships for **a)** as-sintered and air-quenched Mn-AC at 100 kHz **b)** air-quenched Mn-AC at various frequencies **c)** as-sintered Mn-AC samples quenched after annealing at 750°C for 15 min. and 21 h, measured at 100 kHz.

The significant alteration in the ε_r–T characteristics indicates that some inter-diffusion of core and shell phases might have occurred during the extended annealing procedure. On the other hand the pronounced frequency-dependence of ε_r and tanδ in the high temperature region, which are attributed to the effects of increasing electrical conductivity and associated interfacial (space-charge) polarisation mechanisms, could offer an alternative explanation. In this case it may be suggested that the apparent increase in permittivity is actually a result of further volatilisation of bismuth oxide during annealing (Equation 1), which could increase the p-type electronic conductivity according to equation 2. Calculations of the equivalent AC conductivity, σ_{AC}, in the high temperature region indicate that the conductivity was reduced after quenching but increased slightly for the 21 h-annealed sample, as illustrated in Figure S4. Therefore, we suppose that the increase in the dielectric peak height is primarily due to partial inter-diffusion of the core and shell phases during annealing, although the influence of bismuth volatilisation during annealing cannot be completely discounted. Further studies, for example involving electrical impedance measurements at high temperatures, would help to clarify this point.

View Article Online
DOI: 10.1039/C7TC04122E

3.4 Ferroelectric Properties

It is commonly reported that $BiFeO_3$-$BaTiO_3$ ceramics prepared in the absence of additional dopants tend to display rounded ferroelectric hysteresis loops, indicating poor insulation behaviour and high dielectric loss.[30,76] On the other hand, well-saturated hysteresis loops of Mn-doped 75BFBT have been reported in several studies.[30,44,55] In the present work, we observed near-rectangular, tilted and/or constricted P-E hysteresis loops for Mn-doped 75BFBT ceramics, depending on the processing methods and sintering conditions. Representative P-E hysteresis loops are illustrated in Figure 6(a), while the loop parameters are summarised in Table 3. The rounded P-E loops obtained for undoped 75BFBT and excessive MnO_2 (3 mol% MnO_2 added before calcination) doped compositions are also presented in Figure S5 (see the ESI) for comparison.

It is evident that the shape of the P-E loop for Mn-AC was unsaturated when sintered at relatively low temperatures, while a well-saturated P-E loop with a remanent polarisation value, P_r, of 0.27 C m^{-2} was obtained for Mn-BC ceramics under the same conditions. On increasing the sintering temperature, a constriction became apparent in the P-E loops of Mn-AC, suggesting the occurrence of an inhibited domain switching behaviour; similar effects were reported previously in $BiFeO_3$ ceramics.[77] The J-E loops for Mn-AC also exhibited multiple broad switching peaks, in contrast to the single sharp peaks of Mn-BC (Figure S6). On the other hand, a gradual decrease in the remanent polarisation of Mn-BC with increasing sintering temperature is attributed to the volatilisation of bismuth oxide, leading to the formation of Fe-rich secondary phases and a reduction in density (from 97 to 92%). It should be noted that sintering above 1050°C caused a reaction with the alumina support plate, which precluded the use of sintering procedures at temperatures above this level.

View Article Online
DOI: 10.1039/C7TC04122E

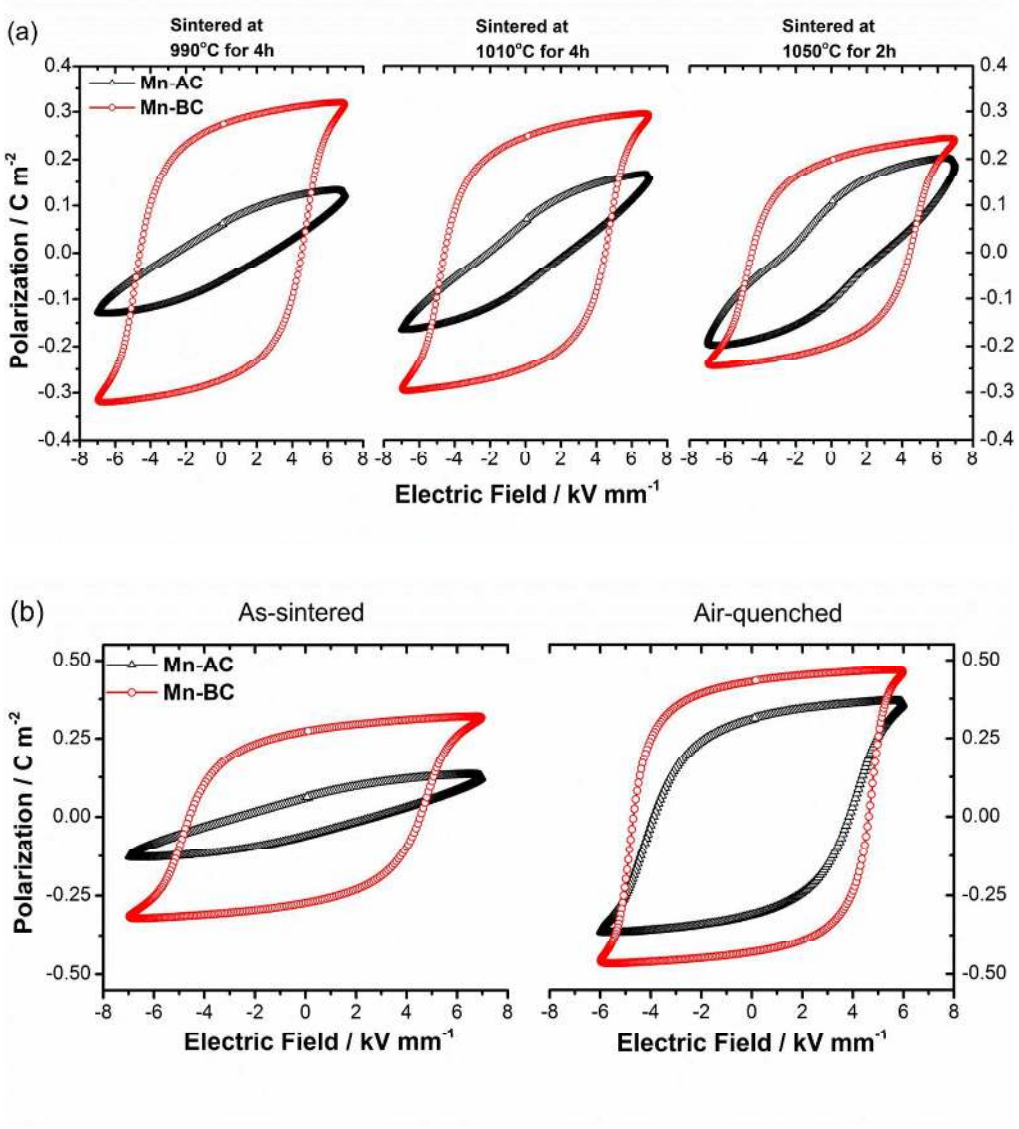

Figure 6. a) Ferroelectric P-E hysteresis loops Mn-AC and Mn-BC ceramics with increasing sintering temperature, **b)** P-E loops of as-sintered (sintered at 990°C for 4h) and air-quenched (annealed at 750°C for 15 min then air-quenched) Mn-doped ceramics.

The occurrence of tilted and/or constricted P-E loops in ferroelectric ceramics can be attributed to several factors[78,79] including domain wall pinning due to oxygen vacancy-cation defect dipoles with related ageing effects,[80,81] the presence of antiferroelectric phases[82,83] or, as reported recently, reversible electric field-induced relaxor ferroelectric to ferroelectric transformations.[84] For undoped $BiFeO_3$ ceramics, it is commonly reported that the constriction phenomenon is associated with 'domain wall pinning' by defect dipoles.[77,85]

Several methods have been reported in the literature to identify the mechanisms responsible for such distorted hysteresis loops, including studies of functional property variations after poling or thermal annealing ('ageing' effects),[86,87] application of a continuous cyclic electric field (field-forced 'deaging'),[77,87] poling at high temperature and thermal quenching. In the present work, it was found that continuous cycling under a high AC electric field (8kV/mm),

View Article Online
DOI: 10.1039/C7TC04122E

either at room temperature or at an elevated temperature of 130°C, did not cause any significant changes in the constricted P-E loops. Therefore, it seems unlikely that a domain wall pinning effect caused by dipolar defect associates could be responsible for such restricted and reversible ferroelectric switching behaviour.

Table 3. Summary of measured ferroelectric P-E loops parameters in the as-sintered and air-quenched Mn-BC and Mn-AC ceramics including remanent polarisation P_r, spontaneous polarisation P_s, and coercive field E_c.

	Sintering conditions			**Air-quenching**
Mn-AC	990°C-4h	1010°C-4h	1050°C-2h	*(from annealing at 750°C-15 min)*
P_r ($C\ m^{-2}$)	0.06	0.07	0.11	0.31
P_s ($C\ m^{-2}$)	0.13	0.17	0.20	0.37
E_c ($kVmm^{-1}$)	2.81	2.46	2.98	3.85
Mn-BC				
P_r ($C\ m^{-2}$)	0.27	0.25	0.22	0.43
P_s ($C\ m^{-2}$)	0.32	0.3	0.26	0.47
E_c ($kVmm^{-1}$)	4.59	4.58	4.53	4.63

On the basis of the microstructural observations in section 3.2 above, we can propose an additional mechanism to restrict ferroelectric domain switching, which has its origin in the core-shell type phase microsegregation, particularly for $BiFeO_3$-rich solid solutions. Due to the compositional variations over the grain, taking the form of core and shell regions, two different solid solutions exist, which have different dielectric and ferroelectric properties. The core region is $BiFeO_3$-rich and exhibits a ferroelectric rhombohedral *R3c* structure while the shell region is $BaTiO_3$-rich and exhibits a pseudo-cubic structure, presumably with relaxor ferroelectric characteristics.[32,72]

One possible explanation is that the reorientation of macroscopic ferroelectric domains in the core is constrained elastically by the nanodomain-structured shell, giving rise to a largely reversible domain switching behaviour. As the high electric field is applied to the core-shell type grains, the macrodomains in the core, which are assumed to be a predominantly rhombohedral structure due to the $BiFeO_3$-rich phase, tend to switch along the electric field direction, resulting in a partial polarisation switching within the grain. However, due to elastic constraint of the core by the shell, the domain switching is partially suppressed giving rise to gradual changes in polarisation over a wide range of electric field strength rather than at a distinct coercive field level. The partially poled core is subject to residual stress upon removal of the electric field, which leads to reversal of the domain switching.

View Article Online
DOI: 10.1039/C7TC04122E

On the other hand, it should be recognised that the shell is likely to contain nano-sized domains, or polar nanoregions (PNRs), which is a signature of relaxor ferroelectric-type materials.[88–90] In view of recent studies on electric field-induced phase transformations in lead-free relaxor ferroelectrics,[84] an alternative explanation for the reversible polarisation switching behaviour can be proposed in which changes in polarisation occur predominantly in the shell region due to electric field-induced relaxor ferroelectric to ferroelectric phase transformations. In this case, the active shell region would be subject to elastic constraint by a relatively inactive $BiFeO_3$-rich ferroelectric core having a high coercive field.

Therefore, the underlying mechanism is most likely based on heterogeneous ferroelectric switching behaviour within the shell and core regions, but at present it is not yet possible to identify which of these is the most active. Elastic interactions between the shell and the core give rise to predominantly reversible ferroelectric switching behaviour. It was reported by Liu *et al.*[91] that the strain and polarisation mismatch can also induce lateral domain nucleation at the interface of the core and shell in $0.75Bi_{0.5}Na_{0.5}TiO_3$-$0.25SrTiO_3$ ceramics. The occurrence of both inter-granular and intra-granular stresses could play an important role in the electro-mechanical fatigue behaviours of these core-shell structured materials, in addition to their influence on the polarisation- and strain-electric field relationships.

The core-shell type microstructure described here for $BiFeO_3$-$BaTiO_3$ ceramics has particular interest due to its influence on the reversibility of the polarisation switching behaviour and the electric field-induced strain. Recently, this type of microstructure has been reported in other Bi-based ferroelectrics.[66,91,67,92] In the case of $0.75Bi_{0.5}Na_{0.5}TiO_3$-$0.25SrTiO_3$, a large unipolar strain output of 0.3% at 4 kV mm^{-1} was attributed to the effects of reversible electric field-driven phase transformations in the shell region. On the other hand, to our knowledge core-shell microstructures have not been reported previously in $BiFeO_3$-$BaTiO_3$ ceramics.

In view of the previous studies on the influence of cooling rate on BF-based ceramics, we performed thermal quenching of the ceramics in air. The influence of such a procedure on the ferroelectric domain switching behaviour is illustrated by the P-E hysteresis loops shown in Figure 6(b). It is evident that quenching greatly improved the polarisation switching behaviour of the ceramics; P_r values of 0.06 and 0.31 C m^{-2} were obtained for the as-sintered and quenched Mn-AC ceramics respectively. The observation of macro-sized ferroelectric domains throughout the grains in the air-quenched Mn-AC specimen, illustrated in Figure 2(f), is directly associated with the enhancement in polarisation switching behaviour. At first sight, thermal quenching appears to eliminate the formation of core-shell structures based on the domain structures that are evident in the micrograph of the chemically-etched Mn-AC ceramic. However, microstructural examination of the air-quenched Mn-AC sample before etching revealed that the chemical inhomogeneity is still present, as shown in Figure S1 (see the ESI). The appearance of domains in the shell region for the air-quenched ceramic, in contrast to the lack of macro-domains in the case of the as-sintered material, indicates differences in ferroelectric ordering within the shell. With slow cooling (as-sintered), the shell tends to be pseudocubic with relaxor ferroelectric nature, while air-quenching transforms the shell into a long range-ordered ferroelectric state which is coherent with the core. Further evidence to support this argument was presented in the section 3.3 above.

View Article Online
DOI: 10.1039/C7TC04122E

It is also worth noting that fast cooling has been reported widely in processing of $BiFeO_3$-based solid solutions as a means to enhance their ferroelectric and piezoelectric properties; the underlying mechanisms are often unclear but usually attributed to ordering of charged defects.[77,93–95] In a recent study by Kim *et al.*[93] on the influence of cooling rate on the properties of undoped $0.75BiFeO_3$-$0.25BaTiO_3$, the beneficial effects of fast cooling procedures were attributed to the influence of oxygen vacancies on the rhombohedral distortion and the transformation to an intermediate orthorhombic phase at high temperatures. In the present case, it is argued that the changes in ferroelectric behaviour are most likely to be associated with nanoscale phase separation, although further evidence (e.g. from TEM studies) is required to support this proposal.

View Article Online
DOI: 10.1039/C7TC04122E

4. CONCLUSIONS

Lead-free $0.75BiFeO_3$-$0.25BaTiO_3$ ferroelectric ceramics were modified by the addition of 1 mol% MnO_2 into either precursor mixed oxide powders (Mn-BC) or undoped calcined powder (Mn-AC). The former incorporation method (Mn-BC) yielded chemically homogeneous materials with saturated P-E ferroelectric hysteresis loops, having a P_r/P_s ratio of 0.84, and a single peak in the dielectric permittivity-temperature relationship indicating a Curie point of approximately 570°C. In contrast, the latter method (Mn-AC) led to the formation of chemically heterogeneous core-shell type microstructures, with constricted P-E hysteresis loops, showing dramatically reduced P_r values and two dielectric anomalies associated with separate phase transitions in the core and shell regions. The temperatures of the peaks in dielectric permittivity were approximately 635 and 480 °C, which are attributed to phase transitions in the core and shell regions respectively. The observation of constricted P-E loops for the Mn-AC BF-BT ceramics is attributed to heterogeneous polarisation switching behaviour in the rhombohedral core and pseudo-cubic shell regions, combined with the effects of elastic constraint. Further work is required to determine which of these regions exhibits the more active polarisation switching characteristics.

The formation of the core-shell structure is attributed to kinetic factors and differences in reactivity during sintering, with the $BiFeO_3$-rich core forming initially and the $BaTiO_3$-rich shell forming at a later stage. Thermodynamic immiscibility between the $BiFeO_3$ and $BaTiO_3$ solid solutions could also play an important role, leading to further nanoscale segregation in the shell region during cooling. Quenching of the BF-BT ceramics in air from a temperature of 750 °C led to significant improvements in ferroelectric switching behaviour. The effects of such a procedure were particularly pronounced for the Mn-AC materials, leading to more clearly-defined peaks in the dielectric permittivity-temperature relationship and the appearance of ferroelectric domain structures within the shell region.

The results of the present study suggest that control of chemical heterogeneity in BF-BT ceramics by manipulation of processing methods and heat treatment procedures could lead to intriguing changes in the electro-mechanical properties associated with different types of ferroelectric switching behaviour. Further investigations of multiferroic/magnetoelectric properties are also warranted as a result of the formation of the multiferroic $BiFeO_3$ phase grain core surrounded by the ferroelectric $BaTiO_3$ solid solution.

Acknowledgements

We thank Diamond Light Source for access to beamline I11 (proposal number EE14061) that contributed to the results presented here. The assistance of Dr Sarah Day and Prof Chiu Tang is gratefully acknowledged. I. Calisir thanks the National Education of Turkish Republic for financial support throughout his PhD.

View Article Online
DOI: 10.1039/C7TC04122E

5. REFERENCES

1. Catalan, G. & Scott, J. F. Physics and Applications of Bismuth Ferrite. *Adv. Mater.* **21,** 2463–2485 (2009).

2. Rojac, T. *et al.* $BiFeO_3$ Ceramics Processing, Electrical, and Electromechanical Properties. *J. Am. Ceram. Soc.* **97,** 1993–2011 (2014).

3. Wang, L., Yang, C.-H. & Wen, J. Physical Principles and Current Status of Emerging Non-Volatile Solid State Memories. *Electron. Mater. Lett.* **11,** 505–543 (2015).

4. Ortega, N., Kumar, A., Scott, J. F. & Katiyar, R. S. Multifunctional magnetoelectric materials for device applications. *J. Phys. Condens. Matter* **27,** 23pp (2015).

5. Zhang, Z., Wu, P., Chen, L. & Wang, J. Density functional theory plus U study of vacancy formations in bismuth ferrite. *Appl. Phys. Lett.* **96,** (2010).

6. Schrade, M., Masó, N., Perejón, A., Pérez-Maqueda, L. A. & West, A. R. Defect chemistry and electrical properties of $BiFeO_3$. *J. Mater. Chem. C* **5,** 10077–10086 (2017).

7. Masó, N. & West, A. R. Electrical properties of Ca-doped $BiFeO_3$ ceramics: From p-type semiconduction to oxide-ion conduction. *Chem. Mater.* **24,** 2127–2132 (2012).

8. Wefring, E. T., Einarsrud, M. & Grande, T. Electrical conductivity and thermopower of (1 - x) $BiFeO_3$ - $xBi_{0.5}K_{0.5}TiO_3$ (x = 0.1, 0.2) ceramics near the ferroelectric to paraelectric phase transition. *Phys. Chem. Chem. Phys.* **17,** 9420–8 (2015).

9. Selbach, S. M., Einarsrud, M. & Grande, T. On the Thermodynamic Stability of $BiFeO_3$. *Chem. Mater.* **21,** 169–173 (2009).

10. Valant, M., Axelsson, A. & Alford, N. Peculiarities of a Solid-State Synthesis of Multiferroic Polycrystalline $BiFeO_3$. *Chem. Mater.* **19,** 5431–5436 (2007).

11. Kumar, M. & Yadav, K. L. Rapid liquid phase sintered Mn doped $BiFeO_3$ ceramics with enhanced polarization and weak magnetization. *Appl Phys Lett* **91,** (2007).

12. Suresh, P. & Srinath, S. Effect of synthesis route on the multiferroic properties of $BiFeO_3$: A comparative study between solid state and sol-gel methods. *J. Alloys Compd.* **649,** 843–850 (2015).

13. Reddy, V. R. *et al.* Reduced leakage current of multiferroic $BiFeO_3$ ceramics with microwave synthesis. *Ceram. Int.* **40,** 4247–4250 (2014).

14. Kumar, M. M., Palkar, V. R., Srinivas, K. & Suryanarayana, S. V. Ferroelectricity in a pure $BiFeO_3$ ceramic. *Appl. Phys. Lett.* **76,** 2764–2766 (2000).

View Article Online
DOI: 10.1039/C7TC04122E

15. Zhang, S., Ma, Y., Awaji, S. & Watanabe, K. Effects of high magnetic field annealing on microstructure and multiferroic properties of $Bi_{1-x}La_xFeO_3$ ceramics. *Ceram. Int.* **42,** 18785–18790 (2016).

16. Yang, C., Kan, D., Takeuchi, I., Nagarajan, V. & Seidel, J. Doping $BiFeO_3$: approaches and enhanced functionality. *Phys. Chem. Chem. Phys.* **14,** 15953–15962 (2012).

17. Walker, J. *et al.* Temperature dependent piezoelectric response and strain–electric-field hysteresis of rare-earth modified bismuth ferrite ceramics. *J. Mater. Chem. C* **4,** 7859–7868 (2016).

18. Yuan, G. L., Or, S. W. & Chan, H. L. W. Structural transformation and ferroelectric – paraelectric phase transition in Bi_{1-x} La_x FeO_3 (x = 0–0.25) multiferroic ceramics. *J. Phys. D. Appl. Phys.* **40,** 1196–1200 (2007).

19. Zhang, L. & Yu, J. Residual tensile stress in robust insulating rhombohedral $Bi_{1-x}La_xFe_{1-y}Ti_yO_3$ multiferroic ceramics and its ability to pin ferroelectric polarization switching. *Appl. Phys. Lett.* **106,** 112907 (2015).

20. Sati, P. C., Arora, M., Chauhan, S., Kumar, M. & Chhoker, S. Effect of Dy substitution on structural , magnetic and optical properties of $BiFeO_3$ ceramics. *J. Phys. Chem. Solids* **75,** 105–108 (2014).

21. Uniyal, P. & Yadav, K. L. Pr doped bismuth ferrite ceramics with enhanced multiferroic properties. *J. Phys.Condens. Matter* **21,** 405901 (2009).

22. Mao, W. *et al.* Effect of Ln (Ln = La , Pr) and Co co-doped on the magnetic and ferroelectric properties of $BiFeO_3$ nanoparticles. *J. Alloys Compd.* **584,** 520–523 (2014).

23. Trivedi, P. *et al.* Modifications in the electronic structure of Rare-Earth doped $BiFeO_3$ multiferroic. *Solid State Commun.* **222,** 5–8 (2015).

24. Bernardo, M. S. *et al.* Intrinsic Compositional Inhomogeneities in Bulk Ti-Doped $BiFeO_3$: Microstructure Development and Multiferroic Properties. *Chem. Mater.* **25,** 1533–1541 (2013).

25. Azough, F. *et al.* Microstructure and properties of Co- , Ni- , Zn- , Nb- and W-modified multiferroic $BiFeO_3$ ceramics. *J. Eur. Ceram. Soc.* **30,** 727–736 (2010).

26. Jun, Y.-K. *et al.* Effects of Nb-doping on electric and magnetic properties in multi-ferroic $BiFeO_3$ ceramics. *Solid State Commun.* **135,** 133–137 (2005).

27. Anjum, G. *et al.* NEXAFS studies of $La_{0.8}Bi_{0.2}Fe_{1-x}Mn_xO_3$ ($0.0 \leq x \leq 0.4$) multiferroic system using x-ray absorption spectroscopy. *J. Phys. D. Appl. Phys.* **44,** 075403 (2011).

View Article Online
DOI: 10.1039/C7TC04122E

28. Kawae, T., Terauchi, Y., Tsuda, H., Kumeda, M. & Morimoto, A. Improved leakage and ferroelectric properties of Mn and Ti codoped $BiFeO_3$ thin films. *Appl Phys Lett* **92,** 112904 (2009).

29. Comyn, T. P., McBride, S. P. & Bell, A. J. Processing and electrical properties of $BiFeO_3$–$PbTiO_3$ ceramics. *Mater. Lett.* **58,** 3844–3846 (2004).

30. Leontsev, S. O. & Eitel, R. E. Dielectric and Piezoelectric Properties in Mn-Modified (1-x)$BiFeO_3$ – x$BaTiO_3$ Ceramics. *J. Am. Ceram. Soc.* **92,** 2957–2961 (2009).

31. Dorcet, V., Marchet, P. & Trolliard, G. Structural and dielectric studies of the $Na_{0.5}Bi_{0.5}TiO_3$ – $BiFeO_3$ system. *J. Eur. Ceram. Soc.* **27,** 4371–4374 (2007).

32. Kiyanagi, R. *et al.* Structural and Magnetic Phase Determination of (1-x)$BiFeO_3$ – x$BaTiO_3$ Solid Solution. *J. Phys. Soc. Japan* **81,** 024603 (2012).

33. Wang, Q. Q., Wang, Z., Liu, X. Q. & Chen, X. M. Improved Structure Stability and Multiferroic Characteristics in $CaTiO_3$-Modified $BiFeO_3$ Ceramics. *J. Am. Ceram. Soc.* **95,** 670–675 (2012).

34. Saad, Y., Alvarez-Serrano, I., Lopez, M. L. & Hidouri, M. Structural and dielectric characterization of new lead-free perovskites in the ($SrTiO_3$)-($BiFeO_3$) system. *Ceram. Int.* **42,** 8962–8973 (2016).

35. Lin, D. *et al.* Microstructure , ferroelectric and piezoelectric properties of $Bi_{0.5}K_{0.5}TiO_3$-modified $BiFeO_3$–$BaTiO_3$ lead-free ceramics with high Curie temperature. *J. Eur. Ceram. Soc.* **33,** 3023–3036 (2013).

36. Yabuta, H. *et al.* Microstructure of $BaTiO_3$ – $Bi(Mg_{1/2}Ti_{1/2})O_3$ – $BiFeO_3$ Piezoelectric Ceramics. *Jpn. J. Appl. Phys.* **51,** 09LD04 (2012).

37. Lee, M. H. *et al.* High-Performance Lead-Free Piezoceramics with High Curie Temperatures. *Adv. Mater.* **27,** 6976–6982 (2015).

38. Sebastian, T. *et al.* High temperature piezoelectric ceramics in the $Bi(Mg_{1/2}Ti_{1/2})O_3$-$BiFeO_3$-$BiScO_3$-$PbTiO_3$ system. *J. Electroceramics* **25,** 130–134 (2010).

39. Rödel, J. *et al.* Transferring lead-free piezoelectric ceramics into application. *J. Eur. Ceram. Soc.* **35,** 1659–1681 (2015).

40. Panda, P. K. Review: environmental friendly lead-free piezoelectric materials. *J. Mater. Sci.* **44,** 5049–5062 (2009).

41. Shrout, T. R. & Zhang, S. J. Lead-free piezoelectric ceramics: Alternatives for PZT? *J. Electroceramics* **19,** 111–124 (2007).

42. Leontsev, S. O. & Eitel, R. E. Progress in engineering high strain lead-free piezoelectric ceramics. *Sci. Technol. Adv. Mater.* **11,** 044302 (2010).

View Article Online
DOI: 10.1039/C7TC04122E

43. Guo, Y. *et al.* Critical roles of Mn-ions in enhancing the insulation, piezoelectricity and multiferroicity of $BiFeO_3$-based lead-free high temperature ceramics. *J. Mater. Chem. C* **3,** 5811–5824 (2015).

44. Liu, X., Xu, Z., Qu, S., Wei, X. & Chen, J. Ferroelectric and ferromagnetic properties of Mn-doped $0.7BiFeO_3$-$0.3BaTiO_3$ solid solution. *Ceram. Int.* **34,** 797–801 (2008).

45. Ye, W., Tan, G., Yan, X., Ren, H. & Xia, A. Influence of Mn dopants on the structure and multiferroic properties of a $Bi_{0.90}Ho_{0.10}FeO_3$ thin film. *RSC Adv.* **5,** 43594–43600 (2015).

46. Kim, D. J. *et al.* Ferroelectric and piezoelectric properties of Mn-modified $BiFeO_3$-$BaTiO_3$ ceramics. *J. Electroceramics* **33,** 37–41 (2014).

47. Joo, H. W., Kim, D. S., Kim, J. S. & Cheon, C. I. Piezoelectric properties of Mn-doped $0.75BiFeO_3$−$0.25BaTiO_3$ ceramics. *Ceram. Int.* **42,** 10399–10404 (2016).

48. Ng, Y. S. & Alexander, S. M. Structural studies of manganese stabilised lead-zirconate-titanate. *Ferroelectrics* **51,** 81–86 (1983).

49. Yoneda, Y., Kitanaka, Y., Noguchi, Y. & Miyayama, M. Electronic and local structures of Mn-doped $BiFeO_3$ crystals. *Phys. Rev. B* **86,** 184112 (2012).

50. Chen, J. & Cheng, J. Enhanced thermal stability of lead-free high temperature $0.75BiFeO_3$–$0.25BaTiO_3$ ceramics with excess Bi content. *J. Alloys Compd.* **589,** 115–119 (2014).

51. Yao, Z. *et al.* Manganese-Doped $BiFeO_3$–$BaTiO_3$ High-Temperature Piezoelectric Ceramics: Phase Structures and Defect Mechanism. *Int. J. Appl. Ceram. Technol.* **13,** 549–553 (2016).

52. Wan, Y. *et al.* Microstructure, Ferroelectric, Piezoelectric, and Ferromagnetic Properties of Sc-Modified $BiFeO_3$ – $BaTiO_3$ Multiferroic Ceramics with MnO_2 Addition. *J. Am. Ceram. Soc.* **97,** 1809–1818 (2014).

53. Li, Q., Cheng, J. & Chen, J. Reduced dielectric loss and enhanced piezoelectric properties of Mn modified $0.71BiFeO_3$–$0.29BaTiO_3$ ceramics sintered under oxygen atmosphere. *J. Mater. Sci. Mater. Electron.* **28,** 1370–1377 (2017).

54. Yang, H. *et al.* Structural , microstructural and electrical properties of $BiFeO_3$ – $BaTiO_3$ ceramics with high thermal stability. *Mater. Res. Bull.* **47,** 4233–4239 (2012).

55. Cen, Z. *et al.* Structural , ferroelectric and piezoelectric properties of Mn-modified $BiFeO_3$-$BaTiO_3$ high-temperature ceramics. *J. Mater Sci Mater Electron* **24,** 3952–3957 (2013).

56. Hang, Q. *et al.* Structural , spectroscopic , and dielectric characterizations of Mn-doped $0.67BiFeO_3$-$0.33BaTiO_3$ multiferroic ceramics. *J. Adv. Ceram.* **2,** 252–259 (2013).

View Article Online
DOI: 10.1039/C7TC04122E

57. Kumar, M. M., Srinivas, A. & Suryanarayana, S. V. Structure property relations in $BiFeO_3/BaTiO_3$ solid solutions. *J. Appl. Phys.* **87,** 855–862 (2000).

58. Mendelson, M. I. Average Grain Size in Polycrystalline Ceramics. *J. Am. Ceram. Soc.* **52,** 443–446 (1969).

59. Stewart, M., Cain, M. G. & Hall, D. Ferroelectric Hysteresis Measurement & Analysis. *NPL Rep. C. 152* 1–57 (1999).

60. Shannon, R. D. Revised Effective Ionic Radii and Systematic Studies of Interatomie Distances in Halides and Chaleogenides. *Acta Cryst.* **A 32,** (1976).

61. Stephens, P. W. Phenomenological model of anisotropic peak broadening in powder diffraction. *J. Appl. Cryst.* **32,** 281–289 (1999).

62. Yasukawa, K. & Nishimura, M. Core–Shell Structure Analysis of $BaTiO_3$ Ceramics by Synchrotron X-Ray Diffraction. *J. Am. Ceram. Soc.* **90,** 1107–1111 (2007).

63. Armstrong, T. R. & Buchanan, R. C. Influence of Core-Shell Grains on the Internal Stress State and Permittivity Response of Zirconia-Modified Barium Titanate. *J. Am. Ceram. Soc.* **73,** 1268–1273 (1990).

64. Lennox, R. C. *et al.* PZT-like structural phase transitions in the $BiFeO_3$–$KNbO_3$ solid solution. *Dalt. Trans.* **44,** 10608–10613 (2015).

65. Dolgos, M. *et al.* Chemical control of octahedral tilting and off-axis A cation displacement allows ferroelectric switching in a bismuth-based perovskite. *Chem. Sci.* **3,** 1426–1435 (2012).

66. Acosta, M. *et al.* Core–Shell Lead–Free Piezoelectric Ceramics: Current Status and Advanced Characterization of the $Bi_{1/2}Na_{1/2}TiO_3$–$SrTiO_3$ System. *J. Am. Ceram. Soc.* **98,** 3405–3422 (2015).

67. Koruza, J. *et al.* Formation of the core – shell microstructure in lead-free $Bi_{1/2}Na_{1/2}TiO_3$-$SrTiO_3$ piezoceramics and its influence on the electromechanical properties. *J. Eur. Ceram. Soc.* **36,** 1009–1016 (2016).

68. Chazono, H. & Kishi, H. Sintering Characteristics in the $BaTiO_3$–Nb_2O_5–Co_3O_4 Ternary System: II, Stability of So-called 'Core–Shell' Structure. *J. Am. Ceram. Soc.* **83,** 101–106 (2000).

69. Sterianou, I., Sinclair, D. C., Reaney, I. M., Comyn, T. P. & Bell, A. J. Investigation of high Curie temperature (1−x) $BiSc_{1-y}Fe_yO_3$ – $xPbTiO_3$ piezoelectric ceramics. *J. Appl. Phys.* **106,** 084107 (2009).

70. Morozov, M. I., Einarsrud, M. A. & Grande, T. Atmosphere controlled conductivity and Maxwell-Wagner relaxation in $Bi_{0.5}K_{0.5}TiO_3$ - $BiFeO_3$ ceramics. *J. Appl. Phys.* **115,** 0–6 (2014).

View Article Online
DOI: 10.1039/C7TC04122E

71. Cao, L. *et al.* Effect of poling on polarization alignment, dielectric behavior, and piezoelectricity development in polycrystalline $BiFeO_3$–$BaTiO_3$ ceramics. *Phys. Status Solidi* **213,** 52–59 (2016).

72. Soda, M., Matsuura, M., Wakabayashi, Y. & Hirota, K. Superparamagnetism Induced by Polar Nanoregions in Relaxor Ferroelectric (1-x)$BiFeO_3$–x$BaTiO_3$. *J. Phys. Soc. Japan* **80,** (2011).

73. Ozaki, T. *et al.* Ferroelectric Properties and Nano-Scaled Domain Structures in (1-x) $BiFeO_3$-x$BaTiO_3$ ($0.33<x<0.5$). *Ferroelectrics* **385,** 6155–161 (2009).

74. Kumari, S. *et al.* Dielectric anomalies due to grain boundary conduction in chemically substituted $BiFeO_3$. *J. Appl. Phys.* **117,** 114102 (2015).

75. Jha, P. K. *et al.* Diffuse phase ferroelectric vs . Polomska transition in (1-x)$BiFeO_3$ - (x)$BaZr_{0.025}Ti_{0.975}O_3$ ($0.1 \leq x \leq 0.3$) solid solutions. *J. Appl. Phys.* **117,** 024102 (2015).

76. Yao, Z. *et al.* Greatly reduced leakage current and defect mechanism in atmosphere sintered $BiFeO_3$ – $BaTiO_3$ high temperature piezoceramics. *J. Mater Sci Mater Electron* **25,** 4975–4982 (2014).

77. Rojac, T., Kosec, M., Budic, B., Setter, N. & Damjanovic, D. Strong ferroelectric domain-wall pinning in $BiFeO_3$ ceramics. *J. Appl. Phys.* **108,** 074107 (2010).

78. Jin, L., Li, F. & Zhang, S. Decoding the Fingerprint of Ferroelectric Loops: Comprehension of the Material Properties and Structures. *J. Am. Ceram. Soc.* **97,** 1–27 (2014).

79. Schenk, T. *et al.* About the deformation of ferroelectric hystereses. *Appl. Phys. Rev.* **1,** 041103 (2014).

80. Yuan, G. L., Yang, Y. & Or, S. W. Aging-induced double ferroelectric hysteresis loops in $BiFeO_3$ multiferroic ceramic. *Appl. Phys. Lett.* **91,** 122907 (2007).

81. Lo, V., Chung, W. W., Cao, H. & Dai, X. Investigating the effect of oxygen vacancy on the dielectric and electromechanical properties in ferroelectric ceramics. *J. Appl. Phys.* **104,** 064105 (2008).

82. Kan, D. *et al.* Universal behavior and electric-field-lnduced structural transition in rare-earth-substituted $BiFeO_3$. *Adv. Funct. Mater.* **20,** 1108–1115 (2010).

83. Tan, X., Ma, C., Frederick, J., Beckman, S. & Webber, K. G. The Antiferroelectric ↔ Ferroelectric Phase Transition in Lead-Containing and Lead-Free Perovskite Ceramics. *J. Am. Ceram. Soc.* **94,** 4091–4107 (2011).

84. Jo, W. *et al.* Giant electric-field-induced strains in lead-free ceramics for actuator applications - Status and perspective. *J. Electroceramics* **29,** 71–93 (2012).

85. Ke, S. *et al.* Tuning of dielectric and ferroelectric properties in single phase $BiFeO_3$ ceramics with controlled Fe^{2+}/ Fe^{3+} ratio. *Ceram. Int.* **40,** 5263–5268 (2014).

View Article Online
DOI: 10.1039/C7TC04122E

86. Carl, K. & Hardtl, K. H. Electrical after-effects in $Pb(Ti,Zr)O_3$ ceramics. *Ferroelectrics* **17,** 473–486 (1977).

87. Genenko, Y. a., Glaum, J., Hoffmann, M. J. & Albe, K. Mechanisms of aging and fatigue in ferroelectrics. *Mater. Sci. Eng. B* **192,** 52–82 (2015).

88. Cross, L. E. Relaxor ferroelectrics: An overview. *Ferroelectrics* **151,** 305–320 (1994).

89. Macutkevic, J., Banys, J., Bussmann-Holder, A. & Bishop, A. R. Origin of polar nanoregions in relaxor ferroelectrics : Nonlinearity , discrete breather formation , and charge transfer. *Phys. Rev. B* **83,** 184301 (2011).

90. Ge, W. *et al.* Direct evidence of correlations between relaxor behavior and polar nano-regions in relaxor ferroelectrics : A case study of lead-free $Na_{0.5}Bi_{0.5}TiO_3$ - x%$BaTiO_3$. *Appl. Phys. Lett.* **103,** 241914 (2013).

91. Liu, N. *et al.* Revealing the core-shell interactions of a giant strain relaxor ferroelectric $0.75Bi_{1/2}Na_{1/2}TiO_3$-$0.25SrTiO_3$. *Sci. Rep.* **6,** 36910 (2016).

92. Ogihara, H., Randall, C. A. & Trolier-McKinstry, S. Weakly Coupled Relaxor Behavior of $BaTiO_3$–$BiScO_3$ Ceramics. *J. Am. Ceram. Soc.* **92,** 110–118 (2009).

93. Kim, D. S., Cheon, C. Il, Lee, S. S. & Kim, J. S. Effect of cooling rate on phase transitions and ferroelectric properties in $0.75BiFeO_3$-$0.25BaTiO_3$ ceramics. *Appl. Phys. Lett.* **109,** 202902 (2016).

94. Lv, J. & Wu, J. Defect dipole-induced poling characteristics and ferroelectricity of quenched bismuth ferrite-. *J. Mater. Chem. C* **4,** 6140–6151 (2016).

95. Kim, S. *et al.* Revealing the role of heat treatment in enhancement of electrical properties of lead-free piezoelectric ceramics. *J. Appl. Phys.* **122,** 014103 (2017).

View Article Online
DOI: 10.1039/C7TC04122E

Table of Content Entry

The formation of core-shell microstructures and ferroelectric switching behaviour in $BiFeO_3$-$BaTiO_3$ ceramics are controlled via dopant incorporation strategies and thermal quenching procedures.